

Special
Issue

Rational Design of a Confacial Pentaoctahedron: Anisotropic Exchange in a Linear $\text{Zn}^{\text{II}}\text{Fe}^{\text{III}}\text{Fe}^{\text{III}}\text{Fe}^{\text{III}}\text{Zn}^{\text{II}}$ Complex

Stephan Walleck,^[a] Mihail Atanasov,^[b, c] Jürgen Schnack,^[d] Eckhard Bill,^[e] Anja Stammler,^[a] Hartmut Bögge,^[a] and Thorsten Glaser^{*,[a]}

Abstract: The first confacial pentaoctahedron comprised of transition metal ions namely $\text{Zn}^{\text{II}}\text{Fe}^{\text{III}}\text{Fe}^{\text{III}}\text{Fe}^{\text{III}}\text{Zn}^{\text{II}}$ has been synthesized by using a dinucleating nonadentate ligand. The face-sharing bridging mode enforces short $\text{Zn}^{\text{II}}\cdots\text{Fe}^{\text{III}}_{\text{A}}$ and $\text{Fe}^{\text{III}}_{\text{A}}\cdots\text{Fe}^{\text{III}}_{\text{B}}$ distances of 2.83 and 2.72 Å, respectively. Ab-initio CASSCF/NEVPT2 calculations provide significant negative zero-field splittings for $\text{Fe}^{\text{III}}_{\text{A}}$ and $\text{Fe}^{\text{III}}_{\text{B}}$ with $|D_{\text{A}}| > |D_{\text{B}}|$ with the main component along the C_3 axis. Hence, a spin-Hamiltonian comprised of anisotropic exchange, zero-field,

and Zeeman term was employed. This allowed by following the boundary conditions from the theoretical results the simulation in a theory-guided parameter determination with $J^y = +0.37$, $J^z = -0.32$, $D_{\text{A}} = -1.21$, $E_{\text{A}} = -0.24$, $D_{\text{B}} = -0.35$, and $E_{\text{B}} = -0.01 \text{ cm}^{-1}$ supported by simulations of high-field magnetic Mössbauer spectra recorded at 2 K. The weak but ferromagnetic $\text{Fe}^{\text{III}}_{\text{A}}\text{Fe}^{\text{III}}_{\text{B}}$ interaction arises from the small bridging angle of 84.8° being at the switch from anti- to ferromagnetic for the face-sharing bridging mode.

Introduction

The interaction between paramagnetic transition metal ions is determined by the bridging mode, the metal-metal and metal-bridging ligand distances. For octahedral coordination, three different bridging modes are possible: corner-sharing, edge-sharing, and face-sharing. The metal-metal distance decreases in this order of bridging motives. The short metal-metal distance in face-sharing octahedra and the resulting strong

electrostatic repulsion between the positively charged metal centers have been supposed to be the origin of the rare occurrence of this bridging motive.^[1,2] On the other hand, this short metal-metal distance enforces a direct overlap of the metal d orbitals corresponding to an onset of a direct metal-metal bonding.^[2]

The bridging of two octahedra in a face-sharing fashion results in a confacial bioctahedron [$\text{L}_3\text{MX}_3\text{ML}_3$] with X being mono-atomic bridging donors.^[1,2] Two ideal octahedra bridged in a face-sharing fashion, representing an ideal bioctahedron, exhibit M-X-M angles of 70.53° .^[1] Deviations from this angle indicate attractive ($< 70.53^\circ$) or repulsive ($> 70.53^\circ$) M...M interactions. A famous example is the complex $[(\text{Me}_3\text{tacn})\text{Fe}(\mu\text{-OH})_3\text{Fe}(\text{Me}_3\text{tacn})]^{2+}$ (Fe-Fe distance of 2.51 Å),^[3,4] which is a class III mixed-valence complex^[5] with a direct $d(z^2)\text{-}d(z^2)$ overlap (Scheme 1a) resulting in a ferromagnetic $S_t = 9/2$ ground state stabilized by a double exchange^[6-8] mechanism. Please note, that in a confacial bioctahedron the quantization axis is along the C_3 axis, i. e. the metal-metal axis.^[1,2]

Confacial trioctahedra – homonuclear and heteronuclear – have been realized using different ligands and synthetic strategies.^[9-19] E. g., the ligand L^{3-} (Scheme 1b)^[14-18] was first reacted to form mononuclear complexes $[\text{LM}^f]^{0,n-}$ as metallo-ligands that can coordinate a third central metal ion M^f by their terminal S_3 facial coordination sites resulting in the confacial trioctahedra. A different synthetic strategy does not require the isolation of the metallo-ligand but generates and reacts it with the central metal ion M^f in situ. This strategy was followed by the reaction of the ligand $\text{H}_3\text{L}'$ (Scheme 1b) with Fe^{II} in a 2:3 ratio to obtain the face-sharing trioctahedron $[(\text{L}')_2\text{Fe}^{\text{III}}_3]^{3+}$.^[19]

Higher nuclearity confacial polyoctahedra are rare. By focusing not only on transition metals, the synthesis and characterization of a confacial tetraoctahedron $\{\text{Co}^{\text{III}}\text{Na}^{\text{I}}\text{Na}^{\text{I}}\text{Co}^{\text{III}}\}$ and a confacial pentaoctahedron $\{\text{Na}^{\text{I}}\text{Co}^{\text{III}}\text{Na}^{\text{I}}\text{Co}^{\text{III}}\text{Na}^{\text{I}}\}$ was described.^[20] In the same line, confacial pentaoctahedra

[a] Dr. S. Walleck, A. Stammler, Dr. H. Bögge, Prof. Dr. T. Glaser
Lehtuhl für Anorganische Chemie I
Fakultät für Chemie
Universität Bielefeld
Universitätsstr. 25, 33615 Bielefeld (Germany)
E-mail: thorsten.glaser@uni-bielefeld.de

[b] Prof. Dr. M. Atanasov
Max-Planck-Institut für Kohlenforschung
Kaiser-Wilhelm-Platz 1, 45470 Mülheim an der Ruhr (Germany)

[c] Prof. Dr. M. Atanasov
Institute of General and Inorganic Chemistry
Bulgarian Academy of Sciences
Akad. G. Bontchev Street, Bl.11, 1113 Sofia (Bulgaria)

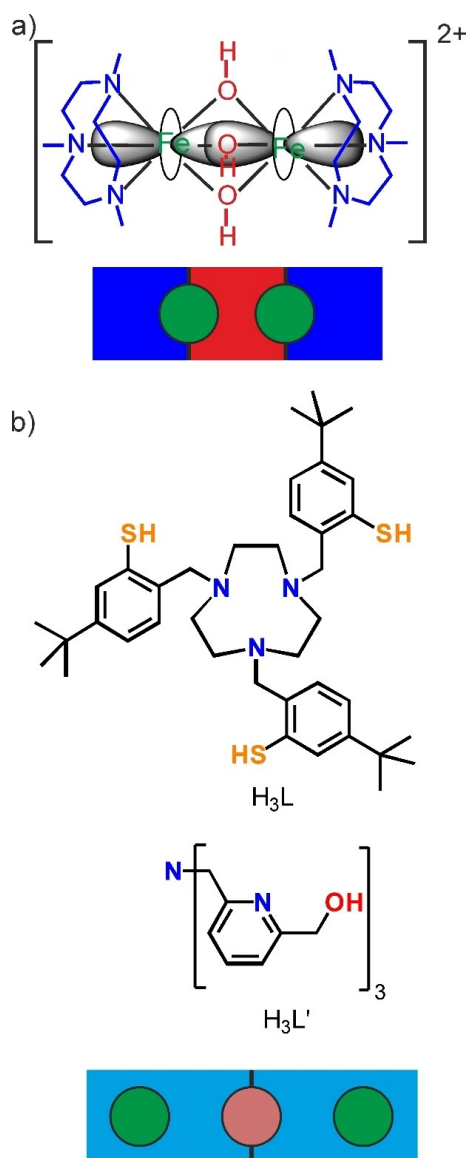
[d] Prof. Dr. J. Schnack
Fakultät für Physik
Universität Bielefeld
Postfach 100131, 33501 Bielefeld (Germany)

[e] Dr. E. Bill
Max-Planck-Institut für Chemische Energiekonversion
Stiftstr. 34–36, 45470 Mülheim an der Ruhr (Germany)

Supporting information for this article is available on the WWW under <https://doi.org/10.1002/chem.202102572>

This manuscript is part of a Special Issue "Cooperative effects in heterometallic complexes".

© 2021 The Authors. Chemistry - A European Journal published by Wiley-VCH GmbH. This is an open access article under the terms of the Creative Commons Attribution Non-Commercial NoDerivs License, which permits use and distribution in any medium, provided the original work is properly cited, the use is non-commercial and no modifications or adaptations are made.

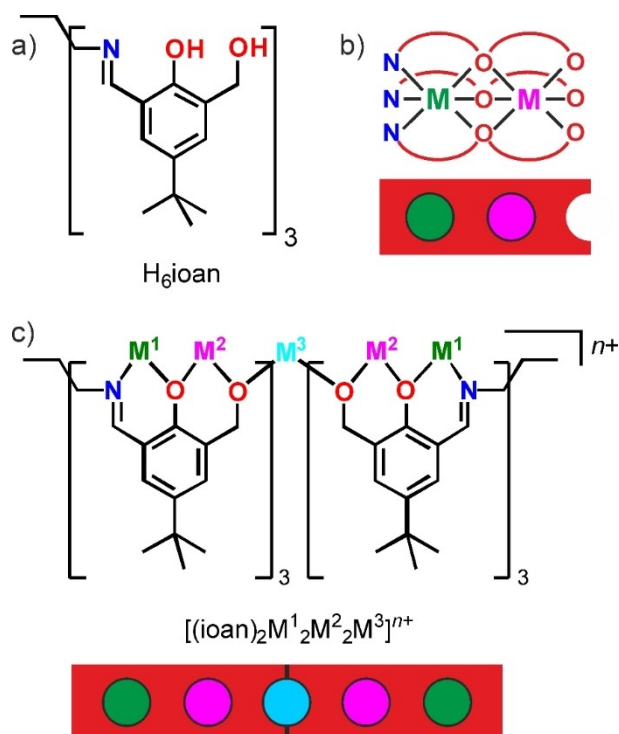


Scheme 1. a) Example of a confacial bioctahedron and b) ligands for the synthesis of confacial trioctahedra.

$\{Mn^II Na^I M^III Na^I Mn^II\}$ with $M^III = Mn^III, Fe^III$ were reported.^[21] Interestingly, two confacial pentaoctahedra of Bi^III were synthesized: a binary iodo bismutate $[Bi^III_5 I_8]^{3-}$ ^[22] and a Bi^III_5 complex with thiolate ligands.^[23] The only known higher-nuclearity complex comprised of transition metals is a confacial nonaocahedron obtained in a self-assembly reaction of Ni^II ions and 1,3-bis-(3-oxo-3-phenylpropionyl)-2-hydroxy-5-methylbenzene.^[24]

Our intention is to obtain a synthetic access to an isostructural series of confacial pentaocahedra that allows the targeted variation of the transition metal center and hence to study the properties of such an unprecedented family of complexes with short metal-metal distances by the face-sharing bridging motive in dependence of the individual d^n electron configurations. Our synthetic strategy implied first the synthesis of confacial bioctahedra^[25] as metallo-ligand building blocks, that can coordinate with one site to a central metal ion in the

second step to provide confacial pentaocahedra. For this reason, we have designed the ligand H_6ioan (Scheme 2a), which provides a N_3O_3 and an O_6 ligand compartment.^[26] The coordinated terminal benzylalcoholato donors should be able to act as bridging ligands, so that two of these metallo-ligand building blocks (Scheme 2b) could coordinate a central metal ion (Scheme 2c). The different donor sets of the two ligand compartments should differentiate the driving force for coordination of individual metal ions. We thought that a more electron-rich metal ion should preferentially coordinate to the N_3O_3 ligand compartment, while the coordination site build by six anionic RO^- donors should be preferentially coordinated by more Lewis acidic metal ions to compensate the strong Lewis nucleophilicity of the three terminal benzylalcoholato donors. In this respect, we could realize the dinuclear complex $[(ioan)Ni^II Ti^IV]$ as the first metallo-ligand building block.^[27] As a *proof-of-principle*, the reaction of this metallo-ligand building block with $[CrCl_3(thf)_3]$ provided the first heterotrinary confacial trioctahedron $[(ioan)Ni^II Ti^IV Cr^III Cl_3]$.^[27] Although the ability of such metallo-ligands to extend the nuclearity in face-sharing octahedra have been proven with this complex, we were not able to obtain such metallo-ligand building blocks without the diamagnetic Ti^IV ion in the O_6 ligand compartment. However, our efforts to obtain such dinuclear metallo-ligand building blocks using either di- or trivalent metal ions, have not been successful yet. We have attributed this to the potential anionic charge of these complexes and the strong basicity of three terminally coordinated benzylalcoholato ligands, which are still too nucleophilic even by being coordinated to a trivalent ion like Fe^III .



Scheme 2. a) The ligand H_6ioan , b) dinuclear metallo ligands capable of coordinating with one facial O_3 side, and c) pentanuclear complexes of face-sharing octahedra.

This raised the question on the necessity to isolate the dinuclear metallo-ligand building blocks $[(\text{ioan})\text{M}^{\text{I}}\text{M}^{\text{II}}]^{n-}$. In this respect, we present herein the in situ synthesis of the confacial pentaoctahedron $[(\text{ioan})_2\text{Zn}^{\text{II}}_2\text{Fe}^{\text{III}}_3]^+$ and its structural, spectroscopic, and magnetic characterization. This complex shows an unexpected ferromagnetic interaction between the high-spin Fe^{III} ions accompanied by anisotropy. The simulation of the magnetic data was guided by DFT and CASSCF/NEVPT2 calculation and required the incorporation of anisotropic exchange and local zero-field tensors.

Results and Discussion

Synthesis

To generate a mononuclear molecular building block in situ, the ligand H_6ioan was treated successively with 1 equiv. Zn^{II} and 3 equiv. NBu_4OMe . The relatively soft Zn^{II} ion should prefer coordination in the N_3O_3 ligand compartment. The coordination of Zn^{II} to the three phenols under these slightly basic conditions should result in some deprotonation but the complete deprotonation of all three phenols is unlikely due to the strong electron-donating character of phenolato ligands and the low Lewis acidity of Zn^{II} ions. In analogy to the reaction of two equivalents of $\text{H}_3\text{L}'$ with 3 equiv. of Fe^{II} under basic conditions,^[19] the in situ generated Zn^{II} complex was added dropwise to a solution of Fe^{II} . This resulted in the deposition of a microcrystalline red solid, which was recrystallized from $\text{CH}_3\text{CN}/\text{Et}_2\text{O}$ providing single-crystals of $[(\text{ioan})_2\text{Zn}_2\text{Fe}_3]\text{ClO}_4 \cdot 1.33\text{CH}_3\text{CN} \cdot 3.33\text{Et}_2\text{O}$ as analyzed by single-crystal X-ray crystallography.

Structural characterization

The asymmetric unit contains a whole complex cation $[(\text{ioan})_2\text{Zn}_2\text{Fe}_3]^+$ (molecule 1 with $\text{Zn1}, \text{Fe2}, \text{Fe3}, \text{Fe4}, \text{Zn5}$, Figure 1a), half of a complex cation (molecule 2 with $\text{Zn6}, \text{Fe7}, \text{Fe8}, \text{Fe7}', \text{Zn6}'$, Figure S1) and five Et_2O and two CH_3CN solvent molecules of crystallization, which results in the formula $[(\text{ioan})_2\text{Zn}_2\text{Fe}_3]\text{ClO}_4 \cdot 1.33\text{CH}_3\text{CN} \cdot 3.33\text{Et}_2\text{O}$ with fractional occupation numbers. The second half of molecule 2 is generated by a center of inversion. The molecular structures of the two molecules do not differ significantly (Figure S2). Selected interatomic distances and angles are provided in Table S1 and thermal ellipsoid plots are provided in Figure S3.

The Zn ions are coordinated in the $\text{N}_3\text{O}^{\text{ph}}_3$ ligand compartments and the Fe ions are coordinated in the $\text{O}^{\text{ph}}_3\text{O}^{\text{bz}}_3$ and in the O^{bz}_6 ligand compartments. From here on, for simplification, the iron ions in the $\text{O}^{\text{ph}}_3\text{O}^{\text{bz}}_3$ ligand compartments are denoted Fe_A (*i.e.* $\text{Fe2}, \text{Fe4}, \text{Fe7}, \text{Fe7}'$) and the iron ions in the O^{bz}_6 ligand compartments are denoted Fe_B (*i.e.* $\text{Fe3}, \text{Fe8}$). As intended, two metallo-ligands $\{(\text{ioan})\text{ZnFe}_A\}$ bind with their facial benzylalcoholato donors a central Fe_B ion to obtain the first transition metal-based confacial pentaoctahedron.

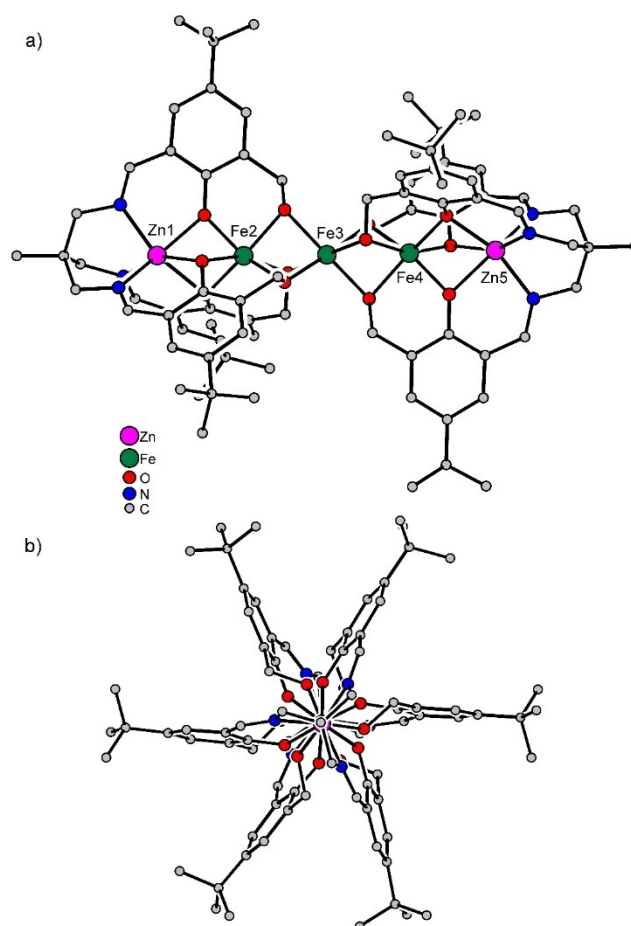


Figure 1. Molecular structure of $[(\text{ioan})_2\text{Zn}_2\text{Fe}_3]^+$ (molecule 1) in single-crystals of $[(\text{ioan})_2\text{Zn}_2\text{Fe}_3](\text{ClO}_4) \cdot 1.33\text{CH}_3\text{CN} \cdot 3.33\text{C}_4\text{H}_{10}\text{O}$ a) perpendicular to the and b) along the approximate C_3 axis. Hydrogen atoms have been omitted for clarity.

$[(\text{ioan})_2\text{Zn}_2\text{Fe}_3]^+$ contains an approximate C_3 axis along the metal-metal vector and an approximate (molecule 1) or crystallographically imposed (molecule 2) center of inversion at Fe_B resulting in an approximate molecular S_6 symmetry (Figure 1). The two $\{(\text{ioan})\text{ZnFe}\}$ metallo-ligands of one molecule form a pair of enantiomers of opposite helical twist (Δ and λ , Figure 2a). This combination of two enantiomers provides a staggered conformation of the benzylic groups (Figure 2b). In contrast, the combination of two metallo-ligands of the same chirality would result in an eclipsed conformation of the benzylic groups that seems sterically not feasible.

The central face-sharing pentaoctahedron core is shown in Figure 3. The M-X-M angles are in the range $84\text{--}88^\circ$ indicating repulsive $\text{Zn}\cdots\text{Fe}$ and $\text{Fe}\cdots\text{Fe}$ forces. In an ideal octahedron, opposite trigonal faces are rotated by 60° against each other (trigonal antiprismatic). These dihedral angles are $\approx 35^\circ$ for the Zn octahedra and $\approx 32^\circ$ for the Fe_A octahedra indicating that the rigid bridging imine-phenolato-benzylalcoholato parts enforce coordination polyhedra that are almost in-between a trigonal prism and a trigonal antiprism. In contrast, the bridging

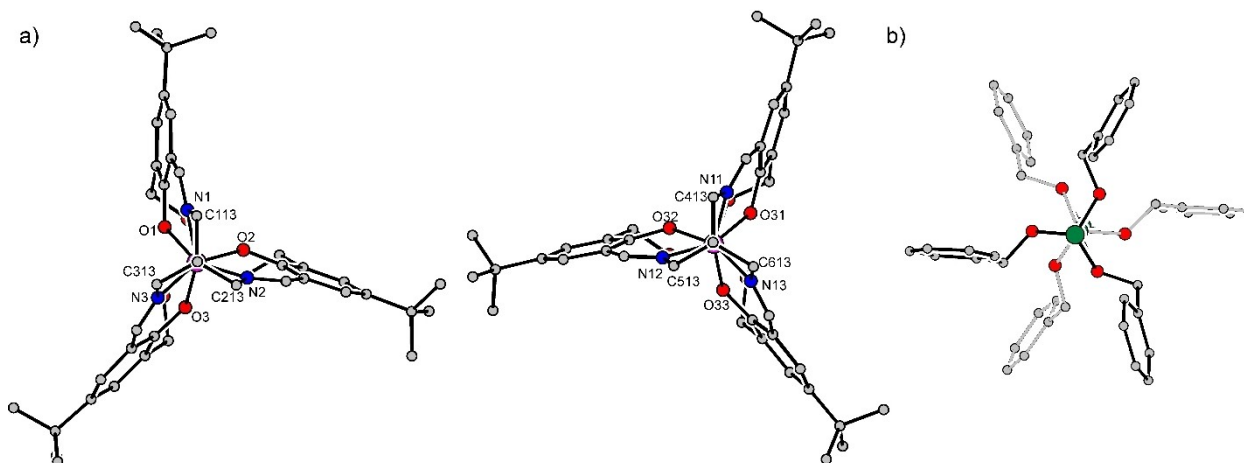


Figure 2. a) Comparison of the two $\{(\text{ioan})\text{ZnFe}\}$ metalloligands of $[(\text{ioan})_2\text{Zn}_2\text{Fe}_3]^+$ molecule 1 with Zn1Fe2 (left) and Zn5Fe4 (right). These substructures are oriented along the C–C bond of the central triimine part of the ligand $(\text{ioan})^{6-}$. The three CH_2 groups are equally oriented with one C oriented straight to the top (C113 and C413). It can be seen that the almost planar phenylimine parts are twisted in the left substructure (N1 and O1) to the left and in the right substructure (N11 and O31) to the right and that this twist direction is the same for the phenylimine parts of each substructure. In this respect, the left substructure is the Δ enantiomer and the right substructure the Δ enantiomer. b) Section of the structure of $[(\text{ioan})_2\text{Zn}_2\text{Fe}_3]^+$ (molecule 1) along the Fe2-Fe3-Fe4 axis to illustrate the staggered orientation of the six benzylic groups (the benzylic part of the back molecular building block drawn with light grey bonds).

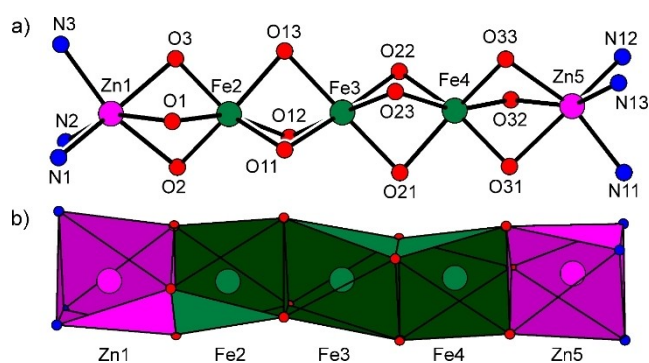


Figure 3. a) Molecular structure and numbering scheme of the metal centers and their donor atoms. b) Polyhedra presentation of the face-sharing pentaoctahedron corresponding to the molecular structure in a).

ligand-free Fe_B octahedron is close (58°) to an ideal trigonal antiprism one.

The twelve negative charges of two $(\text{ioan})^{6-}$ ligands and the cationic nature of $[(\text{ioan})_2\text{Zn}_2\text{Fe}_3]^+$ result in 13 positive charges to be distributed over the five metal ions. Please note that the mean C–O bond lengths of 1.33 \AA for the coordinated phenolates characterize them as innocent phenolato ligands so that no coordinated phenoxyl radicals have to be taken into account.^[28] Assuming the zinc ions to be Zn^{II} , the three iron ions must be Fe^{III} . This assignment is in agreement with the mean metal–ligand bond distances: $d(\text{Zn–N}) = 2.07 \text{ \AA}$, $d(\text{Zn–O}^{\text{ph}}) = 2.16 \text{ \AA}$, $d(\text{Fe}_A\text{–O}^{\text{ph}}) = 2.00 \text{ \AA}$, $d(\text{Fe}_A\text{–O}^{\text{bz}}) = 2.02 \text{ \AA}$, and $d(\text{Fe}_B\text{–O}^{\text{bz}}) = 2.01 \text{ \AA}$. The mean $\text{Zn}\cdots\text{Fe}_A$ and $\text{Fe}_A\cdots\text{Fe}_B$ distances are 2.83 and 2.72 \AA , respectively.

Spectroscopic characterization

The FTIR spectrum of $[(\text{ioan})_2\text{Zn}_2\text{Fe}_3](\text{ClO}_4)$ shows almost the same vibrations as the protonated ligand H_6ioan besides the occurrence of typical features from the ClO_4^- counter ion. The $\nu(\text{C=N})$ vibration is shifted from 1632 to 1626 cm^{-1} in accordance to a coordination of Zn^{II} to the imine donor. The ESI-MS of an CH_3CN solution provides a signal at $m/z = 1662.4$ with an isotope pattern according to $[(\text{ioan})_2\text{Zn}_2\text{Fe}_3]^+$ indicating the stability of this pentanuclear complex in solution. The UV-Vis-NIR spectrum (Figure 4) exhibits intense absorption features above 26000 cm^{-1} mainly from the $\pi\text{-}\pi^*$ transitions of the ligands $(\text{ioan})^{6-}$ and two new strong absorption features around 21200 and 24200 , which are assigned to $\text{RO}^- \rightarrow \text{Fe}^{\text{III}}$ LMCT bands.

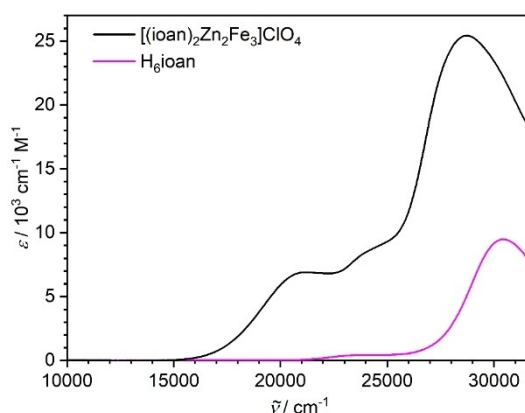


Figure 4. UV-Vis-NIR spectrum of $[(\text{ioan})_2\text{Zn}_2\text{Fe}_3](\text{ClO}_4)$ dissolved in CH_3CN and of the ligand H_6ioan ^[27] for comparison.

The zero-field ^{57}Fe Mössbauer spectrum of $[(\text{ioan})_2\text{Zn}_2\text{Fe}_3](\text{ClO}_4)$ recorded at 80 K (Figure 5a) provides a very asymmetrical single doublet with broadened lines (half-width $> 1 \text{ mm s}^{-1}$). The appearance of the spectrum with non-analytic line shapes indicates intermediate magnetic relaxation in the range of the Mössbauer time scale of 10^{-7} s . Considering the (approximate) S_6 molecular symmetry, two distinct quadrupole doublets would be expected in a 2:1 ratio due to the presence of two almost equal Fe_A sites and a different central Fe_B site.

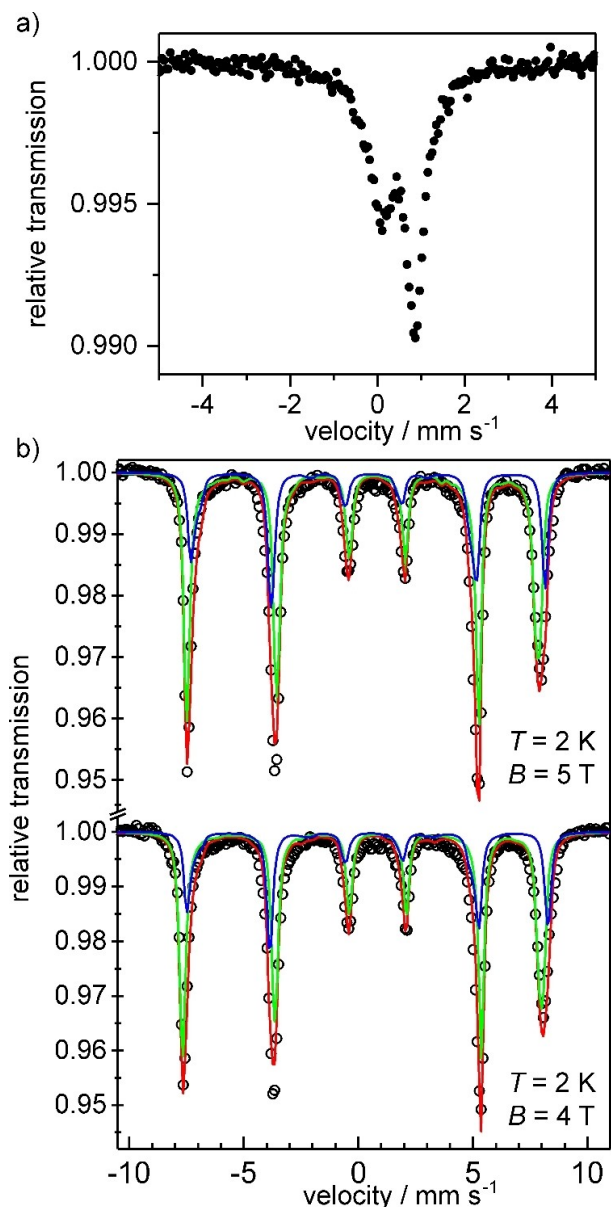


Figure 5. a) Zero-field ^{57}Fe Mössbauer spectrum of $[(\text{ioan})_2\text{Zn}_2\text{Fe}_3](\text{ClO}_4)$ at 80 K. b) Magnetic ^{57}Fe Mössbauer spectra of $[(\text{ioan})_2\text{Zn}_2\text{Fe}_3](\text{ClO}_4)$ at 2 K and applied external field as provided in the figure. The red lines represent the 2:1 superposition of two subspectra obtained with decoupled spins $S_1 = 5/2$, $D_1 = -1.9 \text{ cm}^{-1}$, $E/D_1 = 0.06$, $\delta_1 = 0.51 \text{ mm s}^{-1}$, $\Delta E_{Q,1} = -0.80 \text{ mm s}^{-1}$, $A_{\text{iso},1}/g_N\beta_N = -20.8 \text{ T}$ (green lines), and $S_2 = 5/2$, $D_2 = -0.81 \text{ cm}^{-1}$, $E/D_2 = 0.13$, $\delta_2 = 0.56 \text{ mm s}^{-1}$, $\Delta E_{Q,2} = -0.45 \text{ mm s}^{-1}$, $A_{\text{iso},2}/g_N\beta_N = -21.2 \text{ T}$ (blue lines). For the sake of unambiguity, the g values were kept at 2, the A -tensors were isotropic, the line widths were kept at 0.26 mm s^{-1} , and the efg and D -tensors were taken collinear with asymmetry parameters $\eta = 0$.

Simulation attempts with superposition of two Lorentzian quadrupole doublets did not provide satisfying results. The minima of the transmission lines suggest an average isomer shift $\delta = 0.50 \text{ mm s}^{-1}$ and a quadrupole splitting $|\Delta E_Q| = 0.75 \text{ mm s}^{-1}$ in accordance with Fe^{III} h. s. ions. The apparent similarity of the subspectra indicates, that the different donor sets with six negatively charged RO^- groups (either phenolato or benzylalcoholato) give rise to similar isomer shifts and quadrupole splittings.

In an attempt to separate two Mössbauer signals, spectra were measured in applied magnetic fields at 2 K (Figure 5b). However, again only a single six-line pattern was detected, corroborating Mössbauer-spectroscopic (near) equivalence of the iron ions. The wide magnetic overall splitting of about 14 mm s^{-1} corresponds to internal fields $B_{\text{int}} = -A < S > / g_N\beta_N$ of ca. 43 T, where $< S >$ is the spin expectation value of the system. The high value is typical of Fe^{III} high-spin ions. Accordingly, these high-field magnetic Mössbauer spectra could be reasonably well simulated by adopting local spins $S_i = 5/2$, whereby spin coupling could be completely neglected (Figure S4). As the sharp six-line pattern do not show 'smearing' of the quadrupole shift of lines 1 and 6 vs. 2–5, the angle between internal field and the main component of the electric field gradient tensor (efg) must be fix. Accordingly, negative zero field splitting was invoked, $-D_{\text{av}} \geq 1.3 \text{ cm}^{-1}$, to achieve a corresponding easy axis of magnetization from the low-lying " $m_s = \pm 5/2$ " Kramers doublet. The success of the simple simulation approach with decoupled local spins is in accordance with the moderately weak (ferromagnetic) coupling found below from the analysis of the magnetic data given; the J matrix elements in the range of ca. 1 cm^{-1} are lower than the Zeeman energy at $B = 4 \text{ T}$ giving rise to a splitting of the (local) Kramers m_s -levels by $g\mu_B B \approx 4 \text{ cm}^{-1}$ (for $g = 2$, whereas the effective g_z' value would be even 10 for the $\pm 5/2$ doublet).^[29]

Unfortunately, well resolved magnetic Mössbauer spectra as shown in Figure 5b could be obtained only at base temperature (2 K) with at least moderately strong fields, whereas relaxation broadening persisted at other conditions and prevented us from a full spin-Hamiltonian analysis of the spectra by using their field- and temperature dependence. However, the fact that the single-spin approach of Figure S4 lacks some detail particularly for the outer magnetic hyperfine lines, led us to extend our fit model to two different subspectra in 2:1 ratio, using the zero-field splitting parameters from the magnetic data given below. Again, independent spectra were superimposed, assuming spin decoupling. Optimization of just the isomer shifts, quadrupole splitting, and isotropic magnetic hyperfine coupling tensors yielded nice fits which at least mark the range of possible disparity of the different iron sites in $[(\text{ioan})_2\text{Zn}^{\text{II}}\text{Fe}^{\text{III}}_3]^+$ (Figure 5b). The best fit values are $\delta_A = 0.51 \text{ mm s}^{-1}$, $\Delta E_{Q,A} = -0.80 \text{ mm s}^{-1}$, $A_{\text{iso},A}/g_N\beta_N = 20.8 \text{ T}$ (66.6%), $\delta_B = 0.56 \text{ mm s}^{-1}$, $\Delta E_{Q,B} = -0.45 \text{ mm s}^{-1}$, $A_{\text{iso},B}/g_N\beta_N = 21.2 \text{ T}$ (33.3%).

Magnetic properties

Magnetic data were obtained with powdered samples of $[(\text{ioan})_2\text{Zn}_2\text{Fe}_3]\text{ClO}_4 \cdot \text{H}_2\text{O}$ embedded in eicosane to prevent torquing of the particles (Figure 6). The effective magnetic moment, μ_{eff} (Figure 6a), has a value of $10.28 \mu_{\text{B}}$ at 300 K corresponding to three uncoupled Fe^{III} ($S_i=5/2$) ions (calculated for $g_i=2.00$: $\mu_{\text{eff}}=10.25 \mu_{\text{B}}$). By decreasing the temperature, μ_{eff} increases below 120 K to reach a maximum of $10.50 \mu_{\text{B}}$ at 17 K and then drops to a value of $7.43 \mu_{\text{B}}$ at 2 K. The 'over-shooting' indicates a ferromagnetic coupling between the Fe^{III} ions. The VT VH magnetization (variable temperature – variable field) exhibits a nesting behavior of the iso-field lines (Figure 6b). The

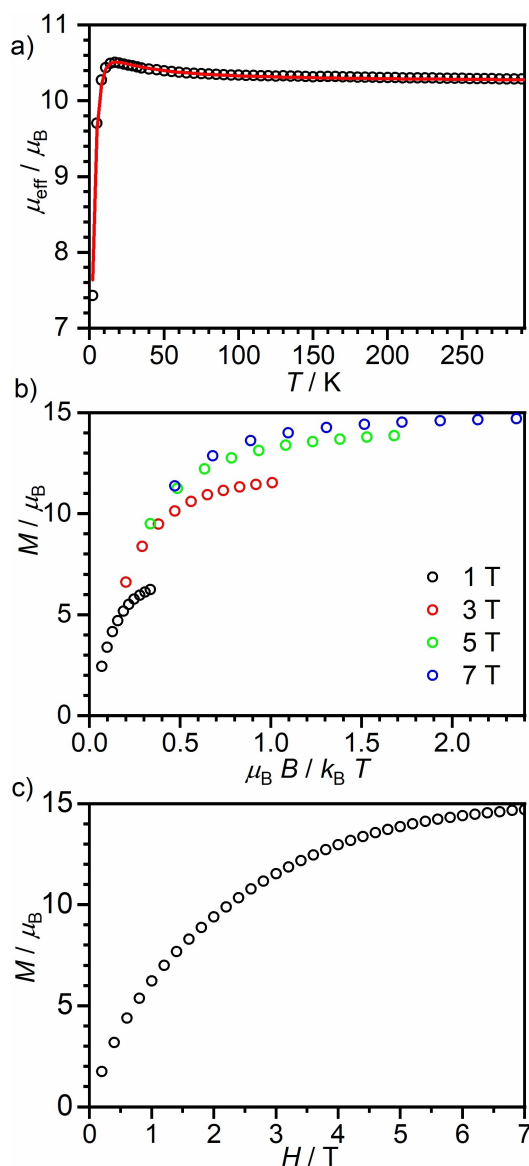


Figure 6. Magnetic data of $[(\text{ioan})_2\text{Zn}_2\text{Fe}_3](\text{ClO}_4) \cdot \text{H}_2\text{O}$ measured in an eicosane matrix: a) Temperature-dependence of the effective magnetic moment, μ_{eff} at 1 T. The red solid line is a simulation to the spin-Hamiltonian Equation (1) with $g_A=g_{A'}=g_B=2.00$, $J_{AB}=0.215 \text{ cm}^{-1}$, $J_{AA'}=-0.13 \text{ cm}^{-1}$, $D_A=3.0 \text{ cm}^{-1}$. b) Variable field-variable temperature (VT VH) magnetizations. c) Field-dependence of the magnetization at 2 K.

field-dependent magnetization of 2 K is shown in Figure 6c. These magnetic data were simulated using the spin-Hamiltonian in Equation (1) consisting of an isotropic Heisenberg-Dirac-van Vleck exchange operator, a local Zeeman term with isotropic g values, and axial local zero-field splitting terms.

$$\hat{H} = -2J_{AB}(\hat{S}_A \cdot \hat{S}_B + \hat{S}_B \cdot \hat{S}_{A'}) - 2J_{AA'}\hat{S}_A \cdot \hat{S}_{A'} + D_A(\hat{S}_{zA}^2 - (1/3)S_A(S_A + 1)) + D_{A'}(\hat{S}_{zA'}^2 - (1/3)S_{A'}(S_{A'} + 1)) + \mu_B g_A \hat{S}_A \cdot \vec{B} + \mu_B g_{A'} \hat{S}_{A'} \cdot \vec{B} + \mu_B g_B \hat{S}_B \cdot \vec{B} \quad (1)$$

The μ_{eff} vs. T data can be simulated with several parameter sets. One such simulation with a not unique parameter set is provided in Figure 6a. However, parameter sets that reproduce the μ_{eff} data could not reproduce the VT VH and 2 K magnetization data. No unique parameter set could be found to reproduce all three magnetic data sets. However, simulations using spin-Hamiltonian Equation (1) indicate a ferromagnetic J_{AB} and significant zero-field splitting parameters.

X-band EPR spectra did not help to resolve the ambiguities of the spin Hamiltonian parametrization of the magnetic properties of $[(\text{ioan})_2\text{Zn}_2\text{Fe}^{\text{III}}_3]^{3+}$ because the competing effects of weak zero-field splitting, spin coupling, and Zeeman splitting in the EPR spectrometer (with microwave energy ca. 0.3 cm^{-1}) led to an unresolvable number of EPR transitions for the three-spin system spreading over a wide field range starting at 10 mT (Figure S5 + S6). The patterns depend significantly on details of g matrices, rhombicities and D tensor orientations. We therefore refrained from further magnetic resonance studies.

In order to understand the origin of the ferromagnetic exchange coupling and the validity of the relatively large absolute values of the zero-field splitting parameters, DFT and multireference ab-initio calculation have been performed.

Ab-initio and DFT calculations

Starting from the molecular structure of $[(\text{ioan})_2\text{Zn}_2\text{Fe}_3]^+$ ab initio CASSCF/NEVPT2 and broken symmetry DFT calculations, respectively, were carried out to probe the local magnetic anisotropy on the two different Fe^{III} spin centers and the isotropic exchange between neighbor (Fe_A-Fe_B) and next-nearest neighbor ($\text{Fe}_A-\text{Fe}_{A'}$) Fe^{III} ions. In these calculations, except for the substitution of two or one Fe^{III} by diamagnetic Ga^{III} ions, respectively, the whole molecular structure of the complex was taken into account without truncations. For comparison, the trigonal complex $[\text{Fe}(\text{cat})_3]^{3-}$ with well documented MCD spectra was included for the analysis of the ab-initio calculations.

The electronic structure of the Fe^{III}_A and Fe^{III}_B ions

For Fe^{III} ions, the d^5 configuration gives rise to one $S=5/2$, 24 $S=3/2$, and 75 $S=1/2$ non-relativistic states, which are further split by spin-orbit coupling. The ab-initio ligand field theory

(AILFT)^[30,31] allows one to deduce all the parameters of the ligand field, the 5×5 ligand field matrix and interelectronic repulsion Racah parameters *B* and *C* from a mapping of a ligand field Hamiltonian onto wave functions and energy eigenvalues (Table 1). Diagonalization of the 5×5 ligand field matrix yields energies of effective 3d-type MOs as plotted in Figure 7. In the case of the complex [Fe(cat)₃]³⁻, the ligand field splitting pattern compare well to the 3d MO level scheme deduced from MCD spectra.^[32]

The LF-MO diagrams for the two Fe^{III} sites in [(ioan)₂Zn₂Fe₃]⁺ show large trigonal splittings of the octahedral *t*₂ parent orbitals, superimposed by a mixing of the two *e* orbitals in the effective trigonal symmetry. It is this mixing which leads to *e*(*t*₂) < *a*₁(*t*₂) (*D*₃ point group notations) for the central Fe^{III}_B site in difference to the Fe^{III}_A terminal sites showing the opposite

Table 1. Ligand field parameters (in cm⁻¹) from an ab-initio ligand field analysis of CASSCF/NEVPT2 wave functions/eigenvalues for [Fe(cat)₃]³⁻ and the ZnGaFeGaZn and ZnFeGaGaZn sites in [(ioan)₂Zn₂Fe₃]⁺ and from MCD (in the case of [Fe(cat)₃]³⁻).

	[Fe(cat) ₃] ³⁻ CASSCF/ NEVPT2	Exp. ^[32]	[(ioan) ₂ Zn ₂ Fe ₃] ⁺ , CASSCF/NEVPT2 ZnGaFeGaZn	ZnFeGaGaZn
10 Dq	12836	13000	14824	11629
Δ <i>t</i> ₂ (<i>D</i> ₃) = <i>e</i> ^a - <i>a</i> ₁	1536	2000	-851	1022
Δ <i>e</i> ^a	0	-	90	143
Δ <i>e</i> ^b	0	-	335	407
<i>B</i>	1066	-	1123	1047
<i>C</i>	3992	-	3870	3935
ζ	444	430	442	441

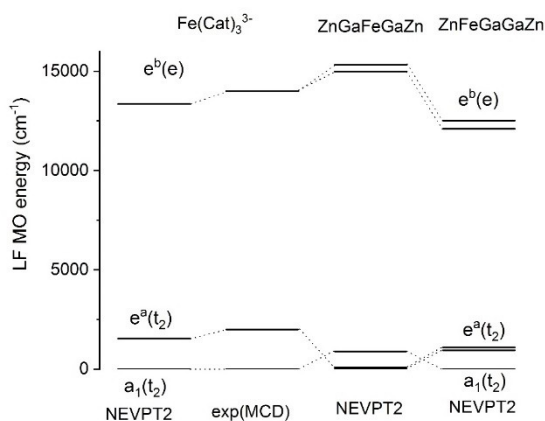


Figure 7. Ab-initio (NEVPT2) 3d-type MOs (ligand field orbitals) for [Fe(cat)₃]³⁻ and the two Fe^{III} sites in [(ioan)₂Zn₂Fe₃]⁺.

Table 2. Bond lengths and polar angles *θ* describing the trigonal distortions in [Fe(cat)₃]³⁻ and the two Fe^{III} sites in [(ioan)₂Zn₂Fe₃]⁺.

	[Fe(cat) ₃] ³⁻	Fe _{central} ^[a]	Fe _{terminal} ^[a]
<i>R</i> _A	2.013	2.009 (OCH ₂ Ph)	1.994(OPH)
<i>R</i> _B		2.009 (OCH ₂ Ph)	2.017(OCH ₂ Ph)
<i>θ</i> _A	55.17	47.88	47.36
<i>θ</i> _B		47.88	47.36

[a] Listed bond angles (in °) and bond lengths (in Å) following an averaging over the six non-equivalent ligands.

order. The exact symmetry of the coordination centers Fe_A and Fe_B is not strictly trigonal and this leads to orthorhombic splittings of the *e*(*t*₂) and *e*(*e*) orbitals. The overall strength of the octahedral component of the ligand field (quantified by 10 Dq) at Fe_B is distinctly larger than that on Fe_A (Table 1). The large trigonal splitting for both Fe_A and Fe_B sites correlate with the rather large angular distortions quantified by the acute values of the (z–Fe–O) polar angles *θ*₁ and *θ*₂ (Table 2) compared to that of a regular octahedron *θ*_{oh} = 54.74°. Energies of the excited *S* = 3/2 state from CASSCF/NEVPT2 calculations along with the parameters *D* and *E* of the spin-Hamiltonian for a *S* = 5/2 ground state are listed in Table 3. Perturbation theory to second order yields expression for *D* in terms of the splitting of the two ⁴T₁ excited states (Eq. (2)) with Δ(⁴A₂) and Δ(⁴E) – the energy separation of the ⁴A₂ and ⁴E excited state from the ⁶A₁ ground state and *ζ*_{eff} – the effective spin-orbit coupling parameter. From the two excited ⁴T₁ states the lowest one dominates the ⁶A₁ splitting. With ⁴A₂ ≥ ⁴E for the lower term ⁴T₁ term (Table 3) negative *D* results which is supported by the calculation. In line with the larger value of 10 Dq for Fe_B, the absolute value |*D*(Fe_B)| is smaller than |*D*(Fe_A)|.

$$D(^4T_1) = \frac{\zeta_{eff}^2}{5} \left[\frac{1}{\Delta(^4A_2)} - \frac{1}{\Delta(^4E)} \right] \quad (2)$$

Correlated calculations based on post-Hartree-Fock methods underestimate the values of *D* of high-spin Fe^{III} complexes due to overestimation of the energies of *S* = 3/2 excited states, especially of the excited ⁴T₁ state because of partial missing of electron correlation. A study of high-spin Fe^{III} tetraphenyl porphyrin complexes allowed a spectroscopic calibration of *D* from CASSCF/NEVPT2 calculations against experimental *D* values from inelastic neutron scattering (INS) to afford one to relate computed *D*(CASSCF/NEVPT2) values with the directly observed ones given by Equation (3).^[33]

$$D(\text{exp, INS}) \cong 5 D(\text{CASSCF/NEVPT2}) \quad (3)$$

Based on the calculations, *D* values for [(ioan)₂Zn₂Fe^{III}]⁺ are estimated at -0.7 cm⁻¹ for Fe^{III}_B and -1.60 cm⁻¹ for Fe^{III}_A and are – along with the *E*/*D* ratios – a good starting approximation for a more sophisticated simulation of the magnetic data.

Table 3. Lowest excited states and zero-field splitting parameters (in cm⁻¹) from CASSCF/NEVPT2 calculations of the central and peripheral Fe^{III} coordination units within the [(ioan)₂Zn₂Fe₃]⁺ complex in comparison with the corresponding values for [Fe(cat)₃]³⁻ with trigonal *D*₃ symmetry.^[32]

Transitions, <i>D</i> ₃ (O)	[Fe(cat) ₃] ³⁻ CASSCF/ NEVPT2	Exp. ^[32]	[(ioan) ₂ Zn ₂ Fe ₃] ⁺ CASSCF/NEVPT2 ZnGaFeGaZn	ZnFeGaGaZn
⁶ A ₁ → ⁴ E(⁴ T ₁ ^a)	18016	10300	15206	17651
			15389	17966
⁶ A ₁ → ⁴ A ₂ (⁴ T ₁ ^a)	18845	11400	15642	20276
⁶ A ₁ → ⁴ E(⁴ T ₁ ^b)	24966	-	22884	25958
			23054	26100
⁶ A ₁ → ⁴ A ₂ (⁴ T ₁ ^b)	25782	-	22020	24744
<i>D</i>	-0.094	-	-0.135	-0.320
<i>E</i> / <i>D</i>	0	-	0.136	0.057

Fe^{III}Fe^{III} exchange couplings. The computation of Fe^{III}Fe^{III} exchange couplings between Fe_A–Fe_B and Fe_A–Fe_A spin-centers using the entire [(ioan)₂Zn₂Fe₃]⁺ complex was technically not possible. To this end, use was made of [(ioan)Zn^{II}Fe^{III}Ga^{III}Zn^{II}(ioan)]⁺ and [(ioan)Zn^{II}Fe^{III}Ga^{III}Fe^{III}Zn^{II}(ioan)]⁺ model complexes derived from the experimentally obtained molecular structure by substitution of one out of the three Fe^{III} ions by a diamagnetic Ga^{III} ion. Computed *J* values obtained by using three different hybrid type functionals (i.e. including exact Hartree-Fock, HF, exchange), the B3LYP (20% HF exchange), TPSS0 (25% HF exchange) and TPSSH (10% HF exchange) are listed in Table 4. Depending on the functional, large both positive (B3LYP, TPSS0) and negative (TPSSH) values of *J*(Fe_A–Fe_B) result, but values of *J*(Fe_A–Fe_A) in all cases are computed relatively small. The experimental magnetic data (see below and above) are only consistent with *J*(Fe_A–Fe_B) exchange couplings that are much smaller than the computed values. Hence, these calculations provide only that *J*(Fe_A–Fe_A) can be neglected.

Simulation of the magnetic data

Supported by the computed single-ion anisotropies of Fe_A and Fe_B as obtained above from spectroscopically-calibrated (CASSCF/NEVPT2) methods, that are quantified by rather large and negative *D* values, and by adopting a weak exchange coupling model ($|D| \gg |J|$) we employed the generic anisotropic spin-Hamiltonian Equation (4) to simulate the three experimental magnetic data sets simultaneously.

$$\begin{aligned} \hat{H} = & -2\hat{S}_A \cdot \begin{pmatrix} J_x & 0 & 0 \\ 0 & J_x & 0 \\ 0 & 0 & J_z \end{pmatrix} \cdot \hat{S}_B - 2\hat{S}_B \cdot \begin{pmatrix} J_x & 0 & 0 \\ 0 & J_x & 0 \\ 0 & 0 & J_z \end{pmatrix} \cdot \hat{S}_A + \hat{S}_A \cdot \\ & \cdot R_z(\varphi_A) \cdot \begin{pmatrix} E_A & 0 & 0 \\ 0 & -E_A & 0 \\ 0 & 0 & D_A \end{pmatrix} \cdot R_z^{-1}(\varphi_A) \cdot \hat{S}_A + \hat{S}_B \cdot R_z(\varphi_B) \cdot \\ & \begin{pmatrix} E_B & 0 & 0 \\ 0 & -E_B & 0 \\ 0 & 0 & D_B \end{pmatrix} \cdot R_z^{-1}(\varphi_B) \cdot \hat{S}_B + \hat{S}_A \cdot R_z(\varphi_A) \cdot \\ & \begin{pmatrix} E_A & 0 & 0 \\ 0 & -E_A & 0 \\ 0 & 0 & D_A \end{pmatrix} \cdot R_z^{-1}(\varphi_A) \cdot \hat{S}_A + \mu_B \vec{B} \cdot \sum_{i=A,B,A'} g_i \hat{S}_i \end{aligned} \quad (4)$$

We use a global coordinate system in which the *J* tensor is diagonal. Very likely in this coordinate system the z-axis points along the approximate molecular C₃ axis. A mirror symmetry is assumed, where the mirror plane situated at Fe_B is perpendicular to the C₃ axis. The *D* tensors are allowed to be rotated about the z-axis by angles φ_A for Fe^{III}_A and φ_B for Fe^{III}_B (rotation matrices *R_z(φ_i)*). Fitting the experimental data with this spin-

Table 4. Isotropic broken symmetry DFT (DKH, D3, RIJCOSX, def2-TZVP, def2-TZVP/J) Fe–Fe exchange coupling parameters (in cm⁻¹, $H_{\text{HDVV}} = -2\hat{S}_1 \cdot \hat{S}_2$ definition) employing various hybrid functionals and the experimentally obtained molecular structure of [(ioan)₂Zn₂Fe₃]⁺.

	B3LYP 20% HF exchange	TPSS0 25% HF exchange	TPSSH 10% HF exchange
ZnFeFeGaZn	3.89	8.13	−4.08
ZnFeGaFeZn	−0.16	−0.05	−0.31
$J = -(E_{\text{HS}} - E_{\text{BS}}) / ((\hat{S}^2)_{\text{HS}} - (\hat{S}^2)_{\text{BS}})^{[46,47]}$			

Hamiltonian provides several independent parameter sets that reproduce the experimental data equally well (Figure 8). All these simulations provide small but anisotropic *J* tensors with an overall ferromagnetic *J*^{iso}. However, the *D* tensors differ significantly. The main component of *D*_i can be along the z axis or rotated into the xy-plane, the sign of *D*_B can be positive or negative, and the absolute value of *D*_i can either be larger for Fe^{III}_A or for Fe^{III}_B. Thus, we employed the results from the ab-initio calculations as boundary conditions for the simulations in a theory-guided parameter determination: (i) main component of *D*_i along the z axis, (ii) *D*_A and *D*_B negative, and (iii) $|D_A| > |D_B|$. This allowed a simulation that provides a good reproduction of the three experimental magnetic data sets (magenta curves in Figure 8) with $J^{\text{xy}} = +0.37$, $J^z = -0.32$, $D_A = -1.21$, $E_A = -0.24$, $D_B = -0.35$, and $E_B = -0.01$ cm⁻¹.

Discussion and Conclusions

The ligand H₆ioan was designed and synthesized for the realization of pentanuclear complexes comprised of octahedral coordination sites that are bridged in a face-sharing fashion, i.e. a face-sharing pentaoctahedron. The preparation was thought to involve the isolation of dinuclear complexes [(ioan)M^IM²]ⁿ⁻ that are treated in a second step with a source of metal ion M³ that becomes coordinated by two [(ioan)M^IM²]ⁿ⁻ molecular building blocks functioning as metallo ligands. However, the strong basicity of the terminally coordinated benzylalcoholato donors prevents the isolation of [(ioan)M^IM²]ⁿ⁻ complexes other than M² being the strong Lewis-acid Ti^{IV}. However, following an in situ approach, we have been able to synthesize the first face-sharing pentaoctahedron [(ioan)₂Zn^{II}₂Fe^{III}₃]⁺ comprised of only transition metal centers presented here.

The molecular structure of [(ioan)₂Zn^{II}₂Fe^{III}₃]⁺ shows significant deviations from an ideal face-sharing pentaoctahedron that would consist of ideal octahedra with a rotation of opposite faces by 60° (trigonal antiprismatic) and bridging angles M–X–M' of 70.53°. The tendency of the sp²-hybridized imine donor parts N=C–C^{ar} to be planar enforces the N₃ and the O^{ph}₃ faces of the Zn^{II} sites to be almost in-between trigonal prismatic and antiprismatic (32–33°). Even more pronounced is the enforcement towards trigonal prismatic (31–32°) by the O^{ph}–C^{ar}–C^{ar}–O^{bz}–O^{bz} bridging chelates of the O^{ph}₃M_AO^{bz}₃ polyhedra. A further distortion is a trigonal elongation of the three

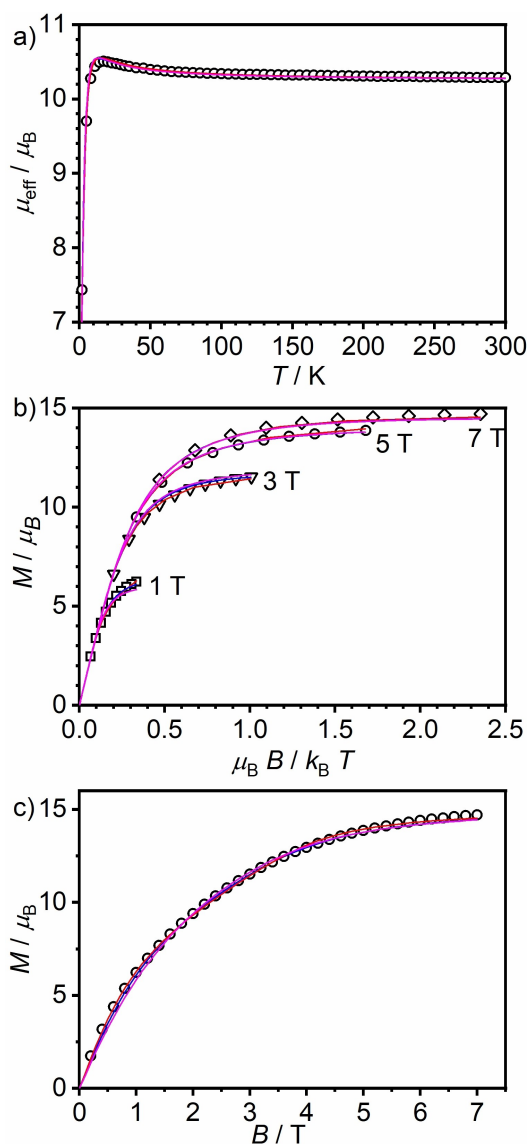


Figure 8. Simulations of the a) temperature-dependence of the effective magnetic moment, μ_{eff} , b) the VTVH magnetization, and c) the field-dependence of the magnetization at 2 K of $[(\text{ioan})_2\text{Zn}_2\text{Fe}_3](\text{ClO}_4) \cdot \text{H}_2\text{O}$ measured in an eicosane matrix (symbols). The solid lines are simulations to the spin-Hamiltonian Equation (4) with three different parameterizations: magenta curves: $J^y = 0.3626$, $J^z = -0.3166$, $D_A = -1.2129$, $E_A = -0.2439$, $D_B = -0.3532$, $E_B = -0.0088 \text{ cm}^{-1}$, $\varphi_A = 114.8^\circ$, $\varphi_B = 1.2^\circ$; red curves: $J^y = +0.4105$, $J^z = -0.3464$, $D_A = -0.2762$, $E_A = -0.3946$, $D_B = -1.7219$, $E_B = -0.0260 \text{ cm}^{-1}$, $\varphi_A = 154.2^\circ$, $\varphi_B = 90.2^\circ$; blue curves: $J^y = +0.3447$, $J^z = -0.2653$, $D_A = -1.1785$, $E_A = +0.1775$, $D_B = -0.5640$, $E_B = +0.5885 \text{ cm}^{-1}$, $\varphi_A = 45.28^\circ$, $\varphi_B = 41.91^\circ$ (please note the magenta curves almost completely cover the red and blue curves).

different coordination sites ($(\text{M}-\text{X}-\text{M}) = 84-88^\circ$) indicating repulsive force between neighboring $\text{M}\cdots\text{M}'$ metal sites. It is difficult to quantify the contribution of the rigid organic ligand backbone to the distortion from ideally face-sharing octahedra (70.53°) but it seems feasible that a significant contribution of the trigonal elongation arises from the rigid ligand backbone. Nevertheless, the face-sharing bridging mode enforces short $\text{M}\cdots\text{M}'$ distances of 2.73 \AA for $\text{Fe}^{\text{III}}_A\cdots\text{Fe}^{\text{III}}_B$ and 2.83 \AA for $\text{Fe}^{\text{III}}_A\cdots\text{Zn}^{\text{II}}$.

An interesting result is the almost same $\text{Fe}^{\text{III}}-\text{O}$ bond length of $2.00-2.02 \text{ \AA}$ for $\text{Fe}^{\text{III}}_A-\text{O}^{\text{ph}}$, $\text{Fe}^{\text{III}}_A-\text{O}^{\text{bz}}$, and $\text{Fe}^{\text{III}}_B-\text{O}^{\text{bz}}$. Generally, a $\text{Fe}^{\text{III}}-\text{O}^{\text{ph}}$ bond is considered to be longer than a $\text{Fe}^{\text{III}}-\text{O}^{\text{bz}}$ bond in a similar coordination environment due to the delocalization of electron density into the aromatic ring, while the electron density of an benzylalcoholate is more localized on oxygen atom that increases the energy of $\text{O}(2p)$ orbitals and hence increase the covalency of the $\text{Fe}^{\text{III}}-\text{O}^{\text{bz}}$ bond relative to the $\text{Fe}^{\text{III}}-\text{O}^{\text{ph}}$ bond. In $[(\text{ioan})\text{Ni}^{\text{II}}\text{Ti}^{\text{IV}}]$ the $\text{Ni}^{\text{II}}-\text{O}^{\text{ph}}$, $\text{Ti}^{\text{IV}}-\text{O}^{\text{ph}}$, and $\text{Ti}^{\text{IV}}-\text{O}^{\text{bz}}$ bond distances are 2.08 , 2.09 , and 1.85 \AA , respectively. Upon coordination of Cr^{III} to the terminal benzylalcoholates, *i.e.* by going to $[(\text{ioan})\text{Ni}^{\text{II}}\text{Ti}^{\text{IV}}\text{Cr}^{\text{III}}\text{Cl}_3]$ these bond distances change significantly to 2.14 , 1.96 , and 1.94 \AA . The increase of the $\text{Ti}^{\text{IV}}-\text{O}^{\text{bz}}$ bond from 1.85 to 1.94 \AA arises from the less electron-donation ability of the benzylalcoholato donors by changing from terminal-to-bridging.^[34] This strongly decreased electron donation of the $\mu_2-\text{O}^{\text{bz}}-\text{Ti}^{\text{IV}}$ bond is compensated by more electron donation of the $\mu_2-\text{O}^{\text{ph}}-\text{Ti}^{\text{IV}}$ bond (going from 2.09 to 1.96 \AA), which in turn reduces the ability of $\mu_2-\text{O}^{\text{ph}}$ to donate charge to Ni^{II} (going from 2.08 to 2.14 \AA). Thus, there is an alternating increase-decrease in metal-ligand bond lengths by coordination of Cr^{III} to the terminal facial O^{bz}_3 donor site.

Such leveling effects also occur in $[(\text{ioan})_2\text{Zn}^{\text{II}}_2\text{Fe}^{\text{III}}_3]^+$. The $\mu_2-\text{O}^{\text{ph}}$ donors have to donate less charge to the more electron-rich Zn^{II} than to the more Lewis-acidic Fe^{III} : $d(\text{Zn}^{\text{II}}-\text{O}^{\text{ph}}) = 2.16 \text{ \AA}$ vs. $d(\text{Fe}^{\text{III}}_A-\text{O}^{\text{ph}}) = 2.00 \text{ \AA}$. This asymmetric $\mu_2-\text{O}^{\text{ph}}$ bonding hence results in a strong electron donation to Fe^{III}_A so that $\mu_2-\text{O}^{\text{bz}}$ can relatively symmetrically donate charge to both Fe^{III}_A (2.02 \AA) and Fe^{III}_B (2.01 \AA). In other words, the similar $\text{Fe}^{\text{III}}_A-\text{O}^{\text{bz}}$ and $\text{Fe}^{\text{III}}_B-\text{O}^{\text{bz}}$ bond lengths result from similar strong charge donor of the remaining three donors to Fe^{III}_A and Fe^{III}_B : the intrinsically strongly donating $\mu_2-\text{O}^{\text{bz}}$ donors for Fe^{III}_B and the especially strong donating $\mu_2-\text{O}^{\text{ph}}$ donors for Fe^{III}_A as they don't have to donate strongly to Zn^{II} . The latter effect is also responsible for the short $\text{Fe}^{\text{III}}_A-\text{O}^{\text{ph}}$ bonds.

The magnetic measurements on $[(\text{ioan})_2\text{Zn}^{\text{II}}_2\text{Fe}^{\text{III}}_3](\text{ClO}_4)$ indicate unexpectedly weak but ferromagnetic interactions in combination to a significant anisotropy. The conventional spin-Hamiltonian Equation (1) with isotropic exchange coupling and axial zero-field splitting is already overparametrized so that inclusion of rhombic zero-field splitting is not justified. Moreover, parameter sets that simulate all three data sets, *i.e.* μ_{eff} vs. T , VTVH, and M vs. H , could not be found. In order to substantiate the relatively strong anisotropy for Fe^{III} h.s. ions and the ferromagnetic couplings as well as to reduce overparametrization, ab-initio and DFT calculation have been performed.

There are many models to reproduce the reported magnetic data. We have used first principle calculations to constrain this ambiguity by making use of local anisotropies as given by ab-initio calculations and keeping, in accordance with the experimental magnetic data showing a weak exchange limit ($|D| \gg |J|$). The results of the ab-initio calculations suggest relatively large and negative D parameters on both Fe^{III} sites with $D_A = -1.60 \text{ cm}^{-1}$ and $D_B = -0.7 \text{ cm}^{-1}$ and the necessity to introduce an anisotropic exchange spin-Hamiltonian. Based on these constraints, a unique parameter set was found in a theory-

guided parameter determination to reproduce all three different experimental data sets which provides anisotropic J and D_i tensors. The axial zero-field splitting parameters are in agreement to the ab-initio results both negative and – in absolute terms – stronger for Fe^{III}_A : $D_A = -1.22 \text{ cm}^{-1}$ and $D_B = -0.35 \text{ cm}^{-1}$ with the main components along the z axis. The anisotropic exchange coupling parameters ($J_z = -0.32$, $J_{xy} = +0.36$, $J_{iso} = +0.20 \text{ cm}^{-1}$) are smaller than the components of the D_i matrices.

It is interesting to interpret the small absolute value of J_{iso} in terms of classical magnetochemistry. The strength of an exchange pathway depends on the covalency ($J \sim \text{covalency}^2$) of the metal-bridging ligand bonds^[35] that is correlated to the metal-bridging ligand bond lengths. The dependence on the angle is less straightforward as there are 25 exchange pathways in a $\text{Fe}^{\text{III}} \text{Fe}^{\text{III}}$ core whose angle-dependence can be averaged out.^[36] In this respect, the famous magneto-structural correlation for $\text{Fe}^{\text{III}}-(\mu\text{-O})-\text{Fe}^{\text{III}}$ complexes of Gorun and Lippard uses only the distance-dependence of the superexchange pathway,^[37] whereas the correlation of Weihe and Güdel explicitly employ the distance- and angular-dependence.^[38] Gatteschi and coworkers found a magneto-structural correlation for $\text{Fe}^{\text{III}}-(\mu\text{-OR})_2-\text{Fe}^{\text{III}}$ complexes that only depends on the bridging angle.^[39] It is interesting to evaluate these magneto-structural correlations together with the complex $[(L')_3\text{Fe}^{\text{III}}_3]^{3+}$, which is the only other linear Fe^{III}_3 complex with face-sharing bridging modes. The magnetic data were fitted with $J_{AB} = -3.1 \text{ cm}^{-1}$ and $J_{AA'} = +0.2 \text{ cm}^{-1}$.^[19] The average bond distances and angles for the bridging pathways are for $[(\text{ioan})\text{Zn}^{\text{II}}_2\text{Fe}^{\text{III}}_3]^+$ ($[(L')_3\text{Fe}^{\text{III}}_3]^{3+}$) 2.026 Å (2.047 Å) and 84.8° (87.6°), respectively. Applying the Gorun-Lippard correlation provides -6.3 cm^{-1} (-4.8 cm^{-1}) and the Weihe-Güdel correlation -15.0 cm^{-1} (-41.9 cm^{-1}). It must be noted that these correlations were obtained for mono-bridged complexes only and therefore the absolute numbers should only be taken as a guideline. The shorter $\text{Fe}^{\text{III}}-\mu\text{-O}$ bond in $[(\text{ioan})\text{Zn}^{\text{II}}_2\text{Fe}^{\text{III}}_3]^+$ should result in a stronger antiferromagnetic interaction in contrast to experiment. In this respect, it is interesting that the angular dependence of the Weihe-Güdel correlation reduces the antiferromagnetic exchange despite the shorter $\text{Fe}^{\text{III}}-\mu\text{-O}$ bond. The linear angular dependence of the Gatteschi and coworkers correlation predicts a switch from antiferromagnetic to ferromagnetic at $\sim 91.2^\circ$ thus providing ferromagnetic exchange for both complexes: $+4.7 \text{ cm}^{-1}$ ($+2.8 \text{ cm}^{-1}$). Thus, although exact numbers should not be taken too seriously, the comparison of both complexes in the light of the three magneto-structural correlations indicates that the small bridging angle of 84.8° is responsible for the small absolute number of J in $[(\text{ioan})\text{Zn}^{\text{II}}_2\text{Fe}^{\text{III}}_3]^+$ defining an experimental switch from antiferromagnetic to ferromagnetic in $\text{Fe}^{\text{III}}-(\mu\text{-OR})_3-\text{Fe}^{\text{III}}$ complexes.

In summary, we have obtained a synthetic access to confacial pentaoctahedra comprised solely by transition metal ions in the central positions by $[(\text{ioan})\text{Zn}^{\text{II}}_2\text{Fe}^{\text{III}}_3]^+$ as a *proof-of-principle*. We are currently working on the synthesis of other confacial pentaoctahedra of the type $[(\text{ioan})\text{M}^1\text{M}^2\text{M}^3\text{M}^2\text{M}^1(\text{ioan})]^{n+}$ with other combinations of M^1 , M^2 , and M^3 especially of mixed-valence type.

Experimental Section

Synthesis

Solvents and starting materials were of the highest commercially available purity. The ligand H_6ioan was synthesized according to the procedure reported previously.^[27] Although we experienced no difficulties, perchlorate salts are potentially hazardous and should only be handled in small quantities and with adequate precautions.

$[(\text{ioan})_2\text{Zn}_2\text{Fe}_3]\text{ClO}_4 \cdot \text{H}_2\text{O}$: A solution of $\text{Zn}(\text{ClO}_4)_2 \cdot 6\text{H}_2\text{O}$ (80 mg, 0.22 mmol, 1.5 equiv.) in MeOH (1 mL) was added to a yellow solution of H_6ioan (99 mg, 0.14 mmol, 1.0 equiv.) in MeOH (3 mL). Addition of a solution of NBu_4OMe in MeOH (20%, 630 mg, 0.46 mmol, 3.2 equiv.) resulted in an orange solution. After stirring for one hour at room temperature, this solution was added dropwise to a solution of $\text{Fe}(\text{ClO}_4)_2 \cdot 6\text{H}_2\text{O}$ (84 mg, 0.23 mmol, 1.6 equiv.) in MeOH (1 mL). The resulting red suspension was stirred for 0.5 h and cooled to 0 °C in order to complete the precipitation. The microcrystalline solid was filtered off and washed three times each with H_2O and Et_2O . Dissolution in MeCN and diffusion of Et_2O led to the deposition of red crystals suited for single-crystal X-ray diffraction. The crystals were filtered off and washed three times each with H_2O and Et_2O . Yield: 59 mg (33 μmol , 47%). IR (KBr): $\nu/\text{cm}^{-1} = 3049 \text{ w}$, 3023 w , 2957 m , 2900 m , 1626 s , 1563 m , 1459 s , 1270 s , 1096 m , 1053 m , 1026 m , 836 m , 763 m , 572 m , 433 m . ESI-MS (MeCN): $m/z = 1662.4$ $[(\text{ioan})_2\text{Zn}_2\text{Fe}_3]^+$. Anal. Calcd. for $[(\text{ioan})_2\text{Zn}_2\text{Fe}_3]\text{ClO}_4 \cdot \text{H}_2\text{O}$, $\text{C}_{82}\text{H}_{104}\text{N}_6\text{O}_{17}\text{ClFe}_3\text{Zn}_2$: C 55.35, H 5.89, N 4.72%. Found: 55.30, H 6.20, N 4.66%.

Crystal structure determination

Single crystals of $[(\text{ioan})_2\text{Zn}_2\text{Fe}_3]\text{ClO}_4 \cdot 1.33\text{CH}_3\text{CN} \cdot 3.33\text{Et}_2\text{O}$ were removed from the mother liquor, coated with oil and immediately cooled to 100(2) K on a Bruker X8 PROSPECTOR ULTRA three-circle diffractometer with 4 K CCD detector, $\text{CuK}\alpha$ radiation, QuazarTM Montel multilayer optics. Empirical absorption corrections using equivalent reflections were performed with the program SADABS-2012/1.^[40] The ratio of minimum to maximum transmission is 0.8401. The structures were solved and refined with the programs SHELXS/L^[41,42] using OLEX2.^[43] Deposition Number 2096283 (for $[(\text{ioan})_2\text{Zn}_2\text{Fe}_3]\text{ClO}_4 \cdot 1.33\text{CH}_3\text{CN} \cdot 3.33\text{Et}_2\text{O}$) contains the supplementary crystallographic data for this paper. These data are provided free of charge by the joint Cambridge Crystallographic Data Centre and Fachinformationszentrum Karlsruhe Access Structures service.

Explanation of CheckCIF A and B Alerts: The asymmetric unit of $[(\text{ioan})_2\text{Zn}_2\text{Fe}_3]\text{ClO}_4 \cdot 1.33\text{CH}_3\text{CN} \cdot 3.33\text{Et}_2\text{O}$ contains 1.5 pentanuclear complexes and a very large solvent accessible void. In the early stages of structure refinement, two MeCN molecules and 5 Et_2O molecules were found in this void. These solvent molecules, however, suffered from strong disorder and could not be refined properly. Therefore, they were handled with by the PLATON/SQUEEZE routine.^[44] The half-occupied perchlorate position is partly disordered with solvent molecules and cannot be modeled properly. To contain the charge balance, counter ions should not be 'squeezed'. Thus, electron density maxima were assigned to correspond to $1/2 \text{ ClO}_4$ (Cl2, Cl3, O5P–O9P). Consequently, this procedure provides meaningless interatomic distances (PLAT430) and angles, which can be ignored. While the disorder could be resolved for one of the *t*-Bu groups (C508–C511), large ellipsoids on carbon atoms of a *t*-Bu group (C408–C411) neighboring the disordered perchlorate clearly indicate, that there is additional unresolved disorder (PLAT213). The disorder also explains the in U-value ratios (PLAT220).

Crystal data for $C_{98}H_{139.33}ClFe_3N_{7.33}O_{19.33}Zn_2$ ($M=2063.23$): monoclinic, space group $P2_1/n$ (no. 14), $a=16.1054(4)$ Å, $b=28.2210(6)$ Å, $c=37.4788(8)$ Å, $\beta=101.6870(10)^\circ$, $V=16681.4(7)$ Å³, $Z=6$, $T=100(2)$ K, $\mu(CuK\alpha)=4.275$ mm⁻¹, $\rho_{calc}=1.232$ g/cm³, crystal size = $0.36 \times 0.33 \times 0.29$ mm³, 183575 reflections measured ($3.95 \leq 2\theta \leq 145.41^\circ$), 32823 unique reflections used in the refinements ($R_{int}=0.0325$). The final R_1 values (1570 refined parameters) were 0.0354 for 30566 reflections with $l > 2\sigma(l)$ and 0.0384 for all data.

Other physical measurements

Infrared spectra (400–4000 cm⁻¹) of solid samples were recorded on a Bruker Vertex 70 as KBr disks. ESI mass spectra were recorded on a Bruker Esquire 3000 ion trap mass spectrometer equipped with a standard ESI source. UV-vis-NIR absorption spectra were measured on a JASCO V770 spectrophotometer at 20 °C. Magnetic susceptibility data were measured on powdered samples in the temperature range 2–300 K by using a SQUID magnetometer (Quantum Design MPMS XL-7 EC) with a field of 1.0 T. Variable-temperature variable-field (VTVH) measurements were performed in various static fields (1–7 T) in the range 2–10 K with the magnetization equidistantly sampled on a $1/T$ temperature scale. For calculations of the molar magnetic susceptibilities, χ_m the measured susceptibilities were corrected for the underlying diamagnetism of the sample holder and the sample by using tabulated Pascal's constants.

⁵⁷Fe Mössbauer spectra were recorded on alternating constant-acceleration spectrometers. The minimal line-width was 0.24 mm s⁻¹ full-width at half-height. ⁵⁷Co/Rh was used as the radiation source. Isomer shifts were determined relative to α -iron at room temperature. The sample temperature was maintained constant either in a bath cryostat (Wissel MBBC-HE0106), or in an Oxford Instruments Mössbauer-Spectromag cryostat. The latter is a split-pair super-conducting magnet system for applied fields up to 8 T where the temperature of the sample can be varied in the range 1.5 K to 250 K. The field is oriented vertically and perpendicular to the horizontal γ -beam. In this system, the ⁵⁷Co/Rh source (1.8 GBq) was positioned at room temperature inside the gap of the magnet at a zero-field position, by using a re-entrant bore tube. The magnetic Mössbauer spectra were simulated with the program MX (by E.B.) by diagonalization of the spin Hamiltonian for $S=5/2$:

$$\hat{H} = g\mu_B \hat{S} \cdot \hat{B} + D[\hat{S}_z^2 - (1/3)S(S+1)] + (E/D)(\hat{S}_x^2 - \hat{S}_y^2) \quad (5)$$

where g is the average electronic g value, and D and E/D are the axial and rhombic zero-field splitting parameters. The hyperfine interaction for ⁵⁷Fe was calculated by using the usual nuclear Hamiltonian.^[45]

Computational procedure

CASSCF/NEVPT2 and broken symmetry DFT calculations were carried out starting from the molecular structure of [(ioan)₂Zn₂Fe₃]ClO₄·1.33MeCN·3.33Et₂O. For at least some simplification only the more symmetric molecule of the asymmetric unit was used (with a special position of the central Fe ion) and *tert*-butyl groups were replaced by hydrogen atoms. Respectively the local magnetic anisotropy on the two different Fe^{III} spin-centers Fe^{III}_A and Fe^{III}_B and the isotropic exchange between neighbor (Fe^{III}_A–Fe^{III}_B) and next-nearest neighbor (Fe^{III}_A–Fe^{III}_A) centers. In these calculations, except for the substitution of, respectively two or one Fe^{III} by diamagnetic Ga^{III} ions, the entire complex geometry (without truncation) was taken into account. For comparison, the trigonal [Fe(cat)₃]³⁻ complex with well documented MCD spectra was included into the

analysis of ab initio part of this project. The Fe^{III} high-spin configuration gives rise to one $S=5/2$, 24 $S=3/2$ and 75 $S=1/2$ non-relativistic states which are further split by spin-orbit coupling. The ab-initio ligand field theory (AIFLT)^[30,31] allows one to deduce all the parameters of the ligand field, the 5×5 ligand field matrix and interelectronic repulsion parameters B and C from a mapping of ligand field Hamiltonian onto wave functions and energy eigenvalues (Table 1). Diagonalization of the 5×5 LF matrix yields energies of effective 3d-type MOs (Figure 7). In the case of the [Fe(cat)₃]³⁻ complex the LF splitting pattern compare well to the 3d-MO level scheme deduced from MCD spectra.^[32]

Acknowledgement

T.G. acknowledge Bielefeld University for financial support. Open Access funding enabled and organized by Projekt DEAL.

Conflict of Interest

The authors declare no conflict of interest.

Keywords: electronic structures · magnetic properties · polynuclear complexes · supramolecular chemistry

- [1] F. A. Cotton, D. A. Ucko, *Inorg. Chim. Acta* **1972**, *6*, 161–172.
- [2] R. H. Summerville, R. Hoffman, *J. Am. Chem. Soc.* **1979**, *101*, 3821–3831.
- [3] S. Druke, P. Chaudhuri, K. Pohl, K. Wiegardt, X. Q. Ding, E. Bill, A. Sawaryn, A. X. Trautwein, H. Winkler, S. J. Gurman, *Chem. Commun.* **1989**, 59–62.
- [4] D. R. Gamelin, E. L. Bominaar, M. L. Kirk, K. Wiegardt, E. I. Solomon, *J. Am. Chem. Soc.* **1996**, *118*, 8085–8097.
- [5] M. B. Robin, P. Day, *Adv. Inorg. Chem. Radiochem.* **1967**, *10*, 247–422.
- [6] C. Zener, *Phys. Rev.* **1951**, *82*, 403–405.
- [7] P. W. Anderson, H. Hasegawa, *Phys. Rev.* **1955**, *100*, 675–681.
- [8] G. Blondin, J.-J. Girerd, *Chem. Rev.* **1990**, *90*, 1359–1376.
- [9] T. Ghosh, K. Natarajan, P. Kumar, S. M. Mobin, *Inorg. Chem.* **2021**, *60*, 2333–2346.
- [10] M. Kouno, N. Kuwamura, T. Konno, *Chem. Commun.* **2021**, *57*, 1336–1339.
- [11] T. Kobayashi, T. Yamaguchi, H. Ohta, Y. Sunatsuki, M. Kojima, N. Re, M. Nonoyama, N. Matsumoto, *Chem. Commun.* **2006**, 1950–1952.
- [12] T. Konno, S. Aizawa, K. Okamoto, J. Hikada, *Chem. Lett.* **1985**, *12*, 1017.
- [13] T. Konno, S. Aizawa, J. Hidaka, *Bull. Chem. Soc. Jpn.* **1989**, *62*, 585.
- [14] T. Beissel, F. Birkelbach, E. Bill, T. Glaser, F. Kesting, C. Krebs, T. Weyhermüller, K. Wiegardt, C. Butzlaff, A. X. Trautwein, *J. Am. Chem. Soc.* **1996**, *118*, 12376–12390.
- [15] T. Glaser, T. Beissel, E. Bill, T. Weyhermüller, V. Schünemann, W. Meyer-Klaucke, A. X. Trautwein, K. Wiegardt, *J. Am. Chem. Soc.* **1999**, *121*, 2193–2208.
- [16] C. Krebs, T. Glaser, E. Bill, T. Weyhermüller, W. Meyer-Klaucke, K. Wiegardt, *Angew. Chem. Int. Ed.* **1999**, *38*, 359–361; *Angew. Chem.* **1999**, *111*, 370–372.
- [17] T. Glaser, F. Kesting, T. Beissel, E. Bill, T. Weyhermüller, W. Meyer-Klaucke, K. Wiegardt, *Inorg. Chem.* **1999**, *38*, 722–732.
- [18] T. Glaser, E. Bill, T. Weyhermüller, W. Meyer-Klaucke, K. Wiegardt, *Inorg. Chem.* **1999**, *38*, 2632–2642.
- [19] G. Guisado-Barrios, Y. Li, A. M. Z. Slawin, D. T. Richens, I. A. Gass, P. R. Murray, L. J. Yellowlees, E. K. Brechin, *Dalton Trans.* **2008**, 551–558.
- [20] N. Duran, W. Clegg, L. Cucurull-Sánchez, R. A. Coxall, H. R. Jiménez, J. M. Moratal, F. Lloret, P. González-Duarte, *Inorg. Chem.* **2000**, *39*, 4821–4832.
- [21] H. Han, J. C. Carozza, Z. Zhou, Y. Zhang, Z. Wei, A. M. Abakumov, A. S. Filatov, Y.-S. Chen, D. J. SantaLucia, J. F. Berry, E. V. Dikarev, *J. Am. Chem. Soc.* **2020**, *142*, 12767–12776.
- [22] S. Pohl, M. Peters, D. Haase, W. Saak, *Z. Naturforsch. B* **1994**, *49*, 741–746.

- [23] J.-X. Chen, X.-Y. Tang, Z.-G. Ren, Y. Zhang, J.-P. Lang, *Eur. J. Inorg. Chem.* **2009**, 2009, 38–41.
- [24] R. Jin, Z.-S. Cai, S. Dai, X.-F. Jiang, L.-M. Zheng, S.-Y. Yu, *Chem. Asian J.* **2016**, 11, 2021–2024.
- [25] T. Glaser, I. Liratzis, T. Lügger, R. Fröhlich, *Eur. J. Inorg. Chem.* **2004**, 2683–2689.
- [26] B. Sonnenburg, I. Liratzis, A. Stämmler, H. Bögge, T. Glaser, *Eur. J. Inorg. Chem.* **2015**, 2015, 912–915.
- [27] B. Sonnenburg, I. Liratzis, A. Stämmler, H. Bögge, T. Glaser, *Eur. J. Inorg. Chem.* **2015**, 2015, 912–915.
- [28] S. N. Brown, *Inorg. Chem.* **2012**, 51, 1251–1260.
- [29] G. Palmer, in: *Physical Methods in Bioinorganic Chemistry* (Ed.: L. Que Jr.), University Science Books, Sausalito, **2000**.
- [30] M. Atanasov, D. Ganyushin, K. Sivalingam, F. Neese, *Struct. Bonding (Berlin)* **2012**, 143, 149–220.
- [31] M. Atanasov, J. M. Zadrozny, J. R. Long, F. Neese, *Chem. Sci.* **2013**, 4, 139–156.
- [32] T. B. Karpishin, M. S. Gebhard, E. I. Solomon, K. N. Raymond, *J. Am. Chem. Soc.* **1991**, 113, 2977–2984.
- [33] S. E. Stavretis, M. Atanasov, A. A. Podlesnyak, S. C. Hunter, F. Neese, Z.-L. Xue, *Inorg. Chem.* **2015**, 54, 9790–9801.
- [34] T. Glaser, B. Hedman, K. O. Hodgson, E. I. Solomon, *Acc. Chem. Res.* **2000**, 33, 859–868.
- [35] T. Glaser, K. Rose, S. E. Shadle, B. Hedman, K. O. Hodgson, E. I. Solomon, *J. Am. Chem. Soc.* **2001**, 123, 442–454.
- [36] R. Hotzelmann, K. Wieghardt, U. Florke, H. J. Haupt, D. C. Weatherburn, J. Bonvoisin, G. Blondin, J. J. Girerd, *J. Am. Chem. Soc.* **1992**, 114, 1681–1696.
- [37] S. M. Gorun, S. J. Lippard, *Inorg. Chem.* **1991**, 30, 1625–1630.
- [38] H. Weihe, H. U. Güdel, *J. Am. Chem. Soc.* **1997**, 119, 6539–6543.
- [39] F. Le Gall, F. F. deBiani, A. Caneschi, P. Cinelli, A. Cornia, A. C. Fabretti, D. Gatteschi, *Inorg. Chim. Acta* **1997**, 262, 123–132.
- [40] SADABS, Bruker AXS Inc., Madison, Wisconsin, USA, **2012**.
- [41] G. M. Sheldrick, *Acta Crystallogr. Sect. A* **2008**, 64, 112–122.
- [42] G. M. Sheldrick, *Acta Crystallogr. Sect. C* **2015**, 71, 3–8.
- [43] O. V. Dolomanov, L. J. Bourhis, R. J. Gildea, J. A. K. Howard, H. Puschmann, *J. Appl. Crystallogr.* **2009**, 42, 339–341.
- [44] A. L. Spek, *Acta Crystallogr. Sect. C* **2015**, 71, 9–18.
- [45] P. Gütllich, E. Bill, A. X. Trautwein, *Mössbauer Spectroscopy and Transition Metal Chemistry*, Springer, New York, **2011**.
- [46] K. Yamaguchi, Y. Takahara, T. Fueno, in: *Applied Quantum Chemistry* (Eds.: V. H. Smith, H. F. Schaefer, K. Morokuma), Springer Netherlands, Dordrecht, **1986**.
- [47] T. Soda, Y. Kitagawa, T. Onishi, Y. Takano, Y. Shigeta, H. Nagao, Y. Yoshioka, K. Yamaguchi, *Chem. Phys. Lett.* **2000**, 319, 223–230.

Manuscript received: July 15, 2021

Accepted manuscript online: August 24, 2021

Version of record online: October 4, 2021